

Three-Phase Reconstruction Reveals How the Microscopic Structure of the Carbon-Binder Domain Affects Ion Transport in Lithium-Ion Batteries

Moritz Kroll,^[a] Sarah L. Karstens,^[a] Marvin Cronau,^[a] Alexandra Höltzel,^[a] Sabine Schlabach,^[b] Nikita Nobel,^[c] Claudia Redenbach,^[c] Bernhard Roling,^{*,[a]} and Ulrich Tallarek^{*,[a]}

The morphology of the electrolyte-filled pore space in lithium-ion batteries is determined by the solid microstructure formed by μm -sized active material particles and the smaller-featured carbon binder domain (CBD). Tomographic reconstructions have largely neglected the CBD, resulting in inadequately defined pore space morphologies at odds with experimental ionic tortuosity values. We present a three-phase reconstruction of a LiCoO_2 composite cathode by focused ion-beam scanning electron microscopy tomography. Morphological analysis proves that the reconstruction, which combines an unprece-

dent volume (20 μm minimum edge length) with the hitherto highest resolution (13.9 \times 13.9 \times 20 nm^3 voxel size), represents the cathode's pore space morphology. Pore-scale diffusion simulations show consideration of the resolved CBD as indispensable to reproduce ionic tortuosity values from electrochemical impedance spectroscopy. Our results reveal the CBD as a convoluted network that dominates the pore space morphology and limits Li^+ transport through tortuous and constricted diffusion pathways.

1. Introduction

Against the rising demand for more efficient and cost-effective lithium-ion batteries (LIBs), the research and development of new materials and battery systems has led to significant progress in recent years.^[1,2] Additionally, the established battery systems offer considerable optimization potential, particularly regarding the morphology of the porous electrodes, which should combine high capacity for Li^+ storage in the active material (AM) with fast Li^+ transport kinetics in the electrolyte-filled pore space.^[3]

Conventional composite electrodes of LIBs are composed of an AM such as LiCoO_2 (LCO), a carbonate-based liquid electrolyte, and electrochemically inactive carbon binder additives.


The carbon's task is to guarantee electronic conduction between the AM particles, including those disconnected from the rest of the network due to volume changes during charge/discharge, and between AM particles and the current collector.^[4] The binder connects the different components and mechanically stabilizes the electrode.^[5] Electrodes typically contain 90–95 wt% AM and 5–10 wt% carbon binder^[6,7] and are obtained from a slurry-coating procedure. A thin slurry film of AM and carbon particles added to a solution of the binder in an organic solvent is applied to the current collector by doctor blading. When the slurry dries, the binder adheres to the surface of the conductive carbon,^[8] forming an interpenetrating porous phase, the carbon-binder domain (CBD). Cross-sectional scanning electron microscopy (SEM) images revealed that the CBD partially fills the interstitial space between the AM particles and spreads over the entire electrode.^[4,9,10] Electrochemical investigations have qualitatively shown that chemical composition and volume fraction of the CBD directly influence charge transport in the porous electrode and the cycling performance of the battery.^[11–15] However, detailed quantitative descriptions of CBD morphology and spatial CBD distribution in electrodes as well as the expected impact on ionic transport and overall battery performance are still rare.^[6,7,16–24]


The microstructure formed by the solid components is the negative of the liquid electrolyte-filled pore space, in which Li^+ transport takes place. AM particles are usually 3–6 μm sized, whereas the size of the conductive carbon particles is up to two orders of magnitude smaller, at 80–100 nm. Consequently, the distance between the AM particles is in the μm -range, but the pore space becomes much smaller in regions pervaded by the CBD. The tortuous nature of the pathways for ion transport is described by the ionic tortuosity τ_{ion} , which is primarily dependent on the porosity ϵ , but also influenced by constrictiv-

[a] M. Kroll, S. L. Karstens, M. Cronau, Dr. A. Höltzel, Prof. B. Roling, Prof. U. Tallarek
Department of Chemistry
Philipps-Universität Marburg
Hans-Meerwein-Strasse 4, 35032 Marburg, Germany
E-mail: roling@staff.uni-marburg.de
tallarek@staff.uni-marburg.de

[b] Dr. S. Schlabach
Institute for Applied Materials (IAM), Institute of Nanotechnology (INT), and Karlsruhe Nano Micro Facility (KNMF)
Karlsruhe Institute of Technology
76344 Eggenstein-Leopoldshafen, Germany

[c] N. Nobel, Prof. C. Redenbach
Department of Mathematics
TU Kaiserslautern
Gottlieb-Daimler-Strasse, 67663 Kaiserslautern, Germany

 Supporting information for this article is available on the WWW under <https://doi.org/10.1002/batt.202100057>

 © 2021 The Authors. Batteries & Supercaps published by Wiley-VCH GmbH. This is an open access article under the terms of the Creative Commons Attribution Non-Commercial NoDerivs License, which permits use and distribution in any medium, provided the original work is properly cited, the use is non-commercial and no modifications or adaptations are made.

ities such as bottlenecks and dead-ends.^[25,26] The ionic tortuosity τ_{ion} quantifies the dependence of the ion transport on the pore space morphology and can be determined electrochemically or through a reconstruction-simulation (RS) approach, where pore-scale diffusion simulations are performed in physically reconstructed electrode structures.^[27,28]

The accuracy of an RS-derived tortuosity value depends critically on the quality and resolution of the reconstruction, which should cover a representative volume of the electrode and resolve each phase adequately. Reconstructions of electrode structures can be obtained from X-ray tomography (XRT) or focused ion-beam scanning electron microscopy (FIB-SEM) tomography. In XRT, large sample volumes ($> 10,000 \mu\text{m}^3$) can be imaged non-destructively in a short time, but the resolution remains in the hundreds-of-nanometers range. As XRT is based on the absorption of X-rays, the method is suited for heavy elements, such as found in the AM particles, but insensitive to light elements, such as present in the CBD.^[29,30] FIB-SEM tomography uses ions (mostly Ga^+) to remove material from the sample slice-by-slice (milling). Between slicing the SEM signal is used to image the cross-sectional surface. Alternate milling and imaging steps are repeated hundreds of times to produce an image stack, from which a representation of the microstructure of the investigated volume can be obtained by 3D interpolation.^[31,32] Volumes with edge lengths of up to $100 \mu\text{m}$ can be reconstructed by FIB-SEM tomography, but the slicing becomes very time consuming for edge lengths $> 10 \mu\text{m}$. The main advantages of FIB-SEM tomography are its high resolution, down to $< 1 \text{ nm}$,^[33] and the availability of all imaging modes of modern electron microscopy.

Studies that compared RS-derived tortuosity values with those obtained from electrochemical impedance spectroscopy (EIS) experiments often found the RS approach to underestimate the ionic tortuosity.^[28,34] The difference between experimental and simulated tortuosity values was particularly large for XRT reconstructions, although the AM phase was accurately represented, which led to the conclusion that the deviation was due to the insufficiently resolved CBD.^[34]

The size difference between the finer-featured CBD and the AM phase poses a particular challenge to three-phase reconstructions of electrodes, which have been pursued by FIB-SEM tomography^[7,17,18,20] and by a combination of tomography and stochastic modelling.^[6,19,35–38] The latter approach requires numerous assumptions and is thus subject to uncertainties, which explains why the assumed microstructure and porosity of the CBD differ significantly between the studies.^[19,37] Direct imaging by FIB-SEM tomography is the best approach to obtain an accurate description of the CBD, because the method provides the necessary resolution and allows the straightforward, contrast-based interpretation of SEM images that enables a robust segmentation of the different phases. But imaging large volumes at high resolution by FIB-SEM tomography requires long measurement times and produces correspondingly large amounts of raw data that have to be processed and analyzed. Hutzenlaub et al.^[16,39] presented a three-phase, FIB-SEM tomography-based reconstruction including the CBD and compared the calculated ionic tortuosity values with electro-

chemical experiments. The resolution of their reconstruction was, however, too low to resolve CBD porosity, so that the (negative) impact of the CBD on Li^+ transport was overestimated. Liu et al.^[17] filled the electrode's pore space with a silicone-based resin and obtained good contrast between the individual phases (without resolving the CBD microstructure and its porosity). Almar et al.^[7] succeeded in direct imaging of all three phases by FIB-SEM tomography over a large volume, but the resolution (30–50 nm) was too close to the feature size of the CBD branches to fully capture the microstructural information.

In this study we attempt a three-phase reconstruction that combines a sufficiently large volume with sufficiently high resolution to obtain an adequate representation of the pore space morphology of an LCO cathode. Assuming the preparation conditions to control the pore space morphology, we prepare a set of LCO cathodes samples using the slurry-coating technique. One sample is investigated by the RS approach, the other samples by EIS. We present our strategy for FIB-SEM tomography and a procedure to obtain a multiscale, multi-phase reconstruction of the cathode sample from the image data. A detailed morphological analysis of the void space is carried out to ascertain that the reconstructed volume is representative of the electrode structure and to obtain a quantitative description of the pore space morphology. Pore-scale diffusion simulations performed in the reconstructed volume deliver a tortuosity value for comparison with the ionic tortuosity determined by EIS from the other cathode samples. The goal of the study is to shed light on the influence of the CBD microstructure on Li^+ transport in LIBs.

2. Results

2.1. Cathode Preparation and Electrochemical Characterization

Using the slurry-coating technique we prepared LCO cathode samples at a typical composition of 90 wt% AM, 5 wt% carbon, and 5 wt% binder. Disc electrodes were cut from the calendared film whose porosity had been adjusted to $\varepsilon \approx 40\%$. A porosity of about 40% was confirmed for all punched electrodes from their respective weight and thickness, which shows that cathodes with reproducible properties were obtained from the film. One cathode sample was cycled using lithium metal as counter electrode to demonstrate that the electrode works properly (Figure S1). After 3.25 cycles, the cathode was removed and prepared for FIB-SEM tomography (see section 2.2). The other samples were used to determine the ionic tortuosity τ_{EIS} of the electrolyte-filled void space by EIS within the framework of the transmission line model (TLM).

The TLM describes the impedance of a straight, cylindrical pore considering ion migration in the electrolyte-filled pore space and double layer formation at the AM-liquid interface.^[40–42] Previous studies have shown the applicability of the TLM to porous electrodes.^[28,43] Through the use of a relatively large amount of conductive carbon (5 wt%) the

electronic resistance of the cathode can be assumed as negligible. For 0% or 100% state-of-charge (ion-blocking conditions), the charge transfer resistance is approximately infinite. The impedance Z for the TLM can then be stated as^[43]

$$Z = \sqrt{\frac{R_{\text{ion}}}{Q_{\text{DL}}(j\omega)^\beta}} \coth\left(\sqrt{R_{\text{ion}}Q_{\text{DL}}(j\omega)^\beta}\right) \quad (1)$$

where R_{ion} is the effective ion transport resistance, Q_{DL} is the constant phase element (CPE) coefficient with its exponent β (to account for deviations from ideal capacitive behavior), j is the imaginary number and ω the angular frequency. From R_{ion} , an effective conductivity for the electrode's pore space σ_{eff} can be calculated. The ionic tortuosity τ_{EIS} then results from the ratio of the electrolyte's bulk conductivity ($\sigma_{\text{bulk}} = 7.93 \text{ mS cm}^{-1}$) for the liquid electrolyte used) and σ_{eff} multiplied with the porosity ε . Using a symmetrical cell setup to acquire EIS spectra ensures that the obtained σ_{eff} values refer only to the pore space of the investigated LCO electrodes.^[44] For a symmetrical cell setup, τ_{EIS} can be calculated according to Equation (2)^[43]

$$\tau_{\text{EIS}} = \frac{\sigma_{\text{bulk}}}{\sigma_{\text{eff}}} \varepsilon = \frac{\sigma_{\text{bulk}} R_{\text{ion}} A}{2d} \varepsilon \quad (2)$$

where A and d denote the mean area and thickness of the electrodes, respectively.

For EIS measurements, six LCO electrodes were combined into three pairs (for the symmetrical cell setup). Figure 1 shows the Nyquist plot acquired for the three electrode pairs. As intended by the preparation protocol, the three electrode pairs

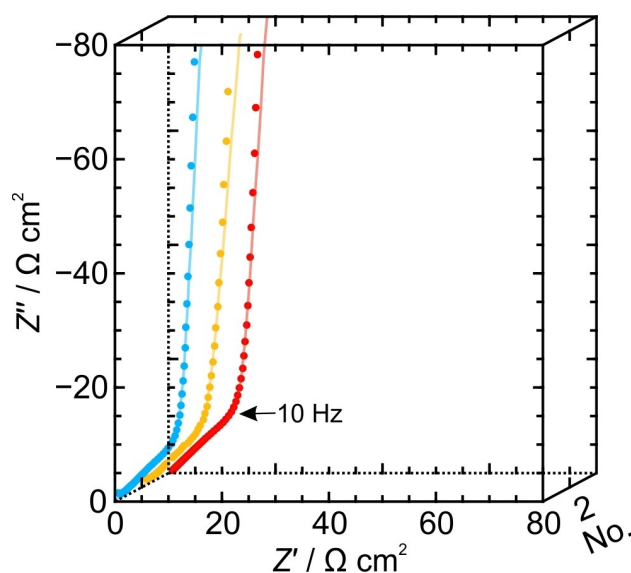


Figure 1. Nyquist plot acquired for symmetrical cells under ion-blocking conditions. The data for the three LCO cathode pairs (no. 1–3) are plotted in the third dimension for better visibility. The resistance of the liquid electrolyte in the separator was subtracted for better comparability of the impedance spectra. As intended, the EIS spectra of all samples show very similar impedances. The TLM (lines) was fitted to the spectra to determine R_{ion} .

showed very similar impedance behavior. Equation 1 was fitted to the spectra to derive R_{ion} values. τ_{EIS} values (Table 1) were then calculated using equation 2 from the R_{ion} values and the values for area, thickness, and porosity determined for the electrodes (Table 1). Averaging over the individual τ_{EIS} values yielded a mean ionic tortuosity of $\tau_{\text{EIS}} = 2.31 \pm 0.20$ (standard deviation). The high standard deviation of τ_{EIS} reflects uncertainties in the experimental determination of the parameters from which τ_{EIS} is calculated, but also hidden variations between the samples, such as small fluctuations in electrode or current collector thickness or slight deteriorations sustained during cell assembly.

2.2. Tomography and Physical Reconstruction

Figure 2 illustrates the workflow from cycling to phase segmentation for the cathode sample selected for the RS approach. After cycling, the cathode sample was prepared for FIB-SEM tomography by filling the pore space with a low-viscosity silicone resin, whose SEM contrast lies between the high-contrast AM particles and the low-contrast CBD branches. The resin-filling performs two important tasks: it increases the contrast between the different phases^[7] and prevents shine-through artifacts from deeper layers.^[47] Vacuum was applied to completely fill even narrow pores within the CBD; unfilled pores were not observed in the tomographic images afterwards. After curing, the sample was embedded in epoxy resin and cut orthogonal to the current collector. The sample was mounted so that the electrode's cross-section was facing upwards. A bulk section from the center of the electrode was selected as the volume-of-interest.

The volume-of-interest and the resolution (slice thickness) are critical to the success of the RS approach in terms of delivering reliable and representative tortuosity values. The edge length of a reconstructed volume must be 20–25 times the average feature size of the phase-of-interest (here the electrolyte-soaked pore space or void phase) to guarantee the absence of finite-size effects.^[48] At the same time, the smallest feature (pores within the CBD) has to be covered by at least 8–10 voxels in each direction to capture its morphology.^[49] From SEM images, the AM particle size was estimated as $\sim 3.5 \mu\text{m}$ and the carbon particle size as 80–120 nm (cf. Figure S2). Due to the adhering binder, the solid CBD branches are thicker than the carbon particles. Based on these discriminative feature sizes

Table 1. Experimental data for the three electrode pairs^[a] used for calculation of τ_{EIS} .

No.	Porosity ε ^[b]	Thickness d [μm]	$R_{\text{ion}} A$ [$\Omega \text{ cm}^2$]	τ_{EIS}
1	40.5%	288	36.5	2.03
2	41.3%	250	36.6	2.39
3	39.5%	238	38.1	2.50

[a] Data reflect the average value from the two electrodes of a pair.
[b] Porosities ε were determined from the weight of the electrodes and densities of the solid components (4.79 g cm^{-3} for LCO,^[45] 1.88 g cm^{-3} for PVDF,^[46] and 1.60 g cm^{-3} for carbon black).

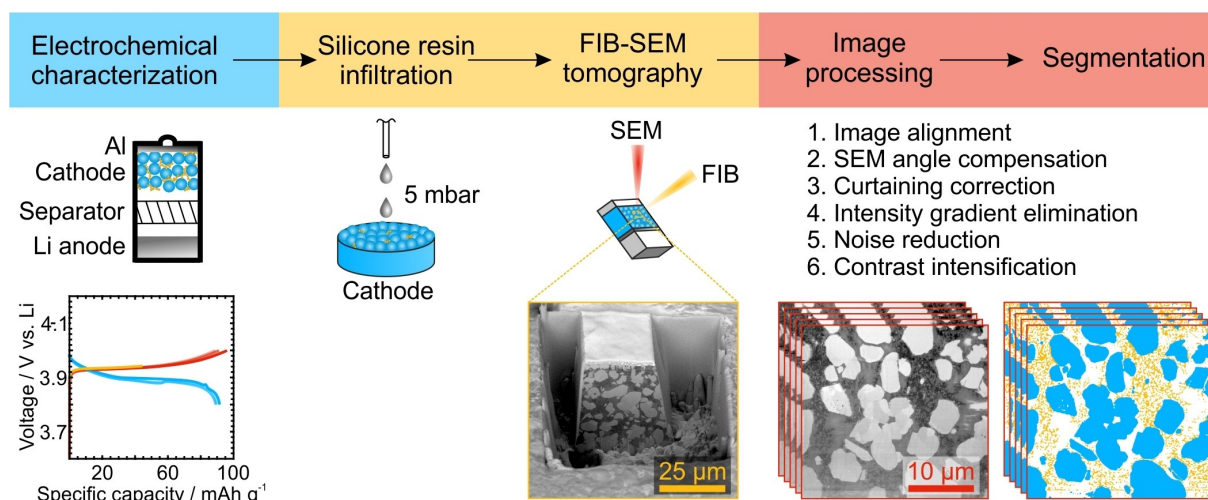


Figure 2. Overview of the workflow from cycling to phase segmentation. One cathode sample was integrated into a battery, using Li metal as anode, and subjected to cycling experiments. After disassembly of the battery, the cathode sample was infiltrated by a low-viscosity silicone resin to enhance the SEM contrast between the different phases, embedded in epoxy resin, and cut to probe the cross-section by FIB-SEM tomography. The resulting image stack was processed following a multi-step routine and segmented into the three different phases: solid AM, solid CBD, and void space.

for the solid components, we estimated an average feature size of $\sim 1 \mu\text{m}$ for the pore space. Therefore, edge lengths of 20–25 μm were targeted for the volume-of-interest, and a slice thickness of 20 nm was chosen for the resolution.

High-resolution imaging was achieved by using the through-the-lens detector (TLD) of the FIB-SEM instrument. This detector was used in backscatter electron mode (TLD-BSE) as the backscattered electrons carry chemical information that can be used to further enhance the contrast (Z or compositional contrast) between the different phases.^[33] A low voltage of 2 kV was applied for a small interaction volume between electron beam and the sample. The information depth of the electron beam was kept small compared to the slice thickness to achieve the highest possible resolution.

After image acquisition, the subsequent image restoration removed artifacts to enable the contrast-based segmentation of the individual phases. Image reconstruction relied heavily on software-supported automation, as the data amount was much too large for an individual post-processing of single images. Typical corrections included in the restoration process were the alignment of the image stack (985 slices) and the compensation of brightness gradients, local charging, and noise. Curtaining artifacts, which are caused by unevenness on the cross-sectional surface,^[31] were a major issue. Each material interacts differently with the ion beam leading to individual sputter rates. The examined composite electrode exhibits numerous material interfaces between solid AM, solid CBD, and silicone resin, thus leading to local changes of beam milling. Curtaining produces stripes that run like a waterfall from top to bottom of an image, becoming more pronounced towards the bottom. The stripes had to be carefully corrected to prevent a considerable loss of resolution. The results of FIB-SEM tomography and image restoration are shown in Figure 3a for the complete reconstructed volume of $26.4 \times 24.5 \times 19.7 \mu\text{m}^3$.

2.3. Morphological Analysis

The three-phase physical reconstruction of the LCO cathode sample shown in Figure 3a is a direct image of the cathode's morphology within the limits of the achieved resolution. The microstructural properties of the electrolyte-filled pore space (void space) correspond to real bulk conditions (as probed by EIS) insofar as the reconstruction is accurate and representative. In the following morphological analysis, this representation is referred to as case I. Although the reconstruction process itself is quite complex, the results can be easily manipulated afterwards to create or isolate structures inaccessible to experiments. Taking advantage of this possibility, we reassigned voxels belonging to the solid CBD as void voxels to simulate the results of a two-phase reconstruction where the CBD was not taken into account (Figure 3b, case II). This representation serves as reference to evaluate the contribution of the CBD to the overall morphology and transport properties of the electrode. The sub-volume shown in Figure 3c corresponds to the largest section occupied by the porous CBD in the reconstructed volume. Analysis of this sub-volume (case III) focuses on the morphology of the CBD. The selected sub-volume represents CBD porosity and feature size, as ascertained by probing the (smaller) porous CBD subsections in the reconstructed volume.

2.3.1. Evaluation of Phase Fractions

Prior to deriving values for morphological descriptors, we assess whether the three-phase reconstruction (case I) recovers the composition of the cathode sample. Table 2 lists the different volume fractions in the reconstruction, determined as the ratio between the number of voxels assigned to a particular phase or feature and the total number of voxels in the

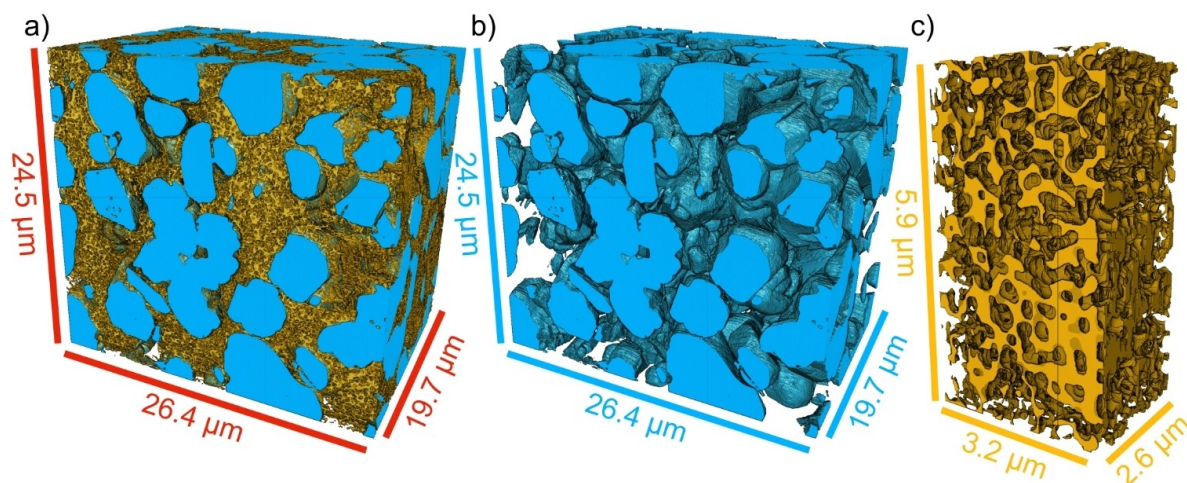


Figure 3. a) 3D representation of the total reconstructed volume of a bulk section of the LCO cathode (solid AM, solid CBD, and void phase in blue, orange, and transparent, respectively). For morphological analysis, this representation is referred to as case I. b) Representation of the reconstructed volume in which solid CBD voxels were replaced by void voxels to simulate the results of imaging without resolution of the CBD (case II). c) Extracted section from the reconstructed volume completely filled by the porous CBD (case III).

Table 2. Reconstruction-derived volume fractions vs cathode sample composition.

Phase	Reconstruction	Cathode sample
Solid AM	48.5 vol% (92.0 wt%) ^[a]	90.0 wt%
Solid CBD	11.5 vol% (8.0 wt%) ^[a]	10.0 wt%
Total void	40.0 vol%	40.8%
Void inside CBD	17.5 vol%	–
Void outside CBD	22.5 vol%	–
Porous CBD (solid and void)	29.0 vol%	–

[a] Wt% calculated from vol% by multiplication with the respective densities (4.79 g cm⁻³ for LCO,^[45] 1.88 g cm⁻³ for PVDF,^[46] and 1.60 g cm⁻³ for carbon black).

reconstruction. Multiplication with the respective density converts the volume fractions of the solid components into weight fractions. The reconstruction-derived weight fractions for the solid AM and CBD phases closely approach the respective weight fractions of the solid components used in cathode preparation. The porosity of the cathode sample of $\epsilon = 40.8\%$, experimentally determined as for the cathode samples used for EIS (Table 1), is also recovered by the void voxel fraction of the reconstructed volume (40.0%).

Having ascertained that case I recovers the phase fractions of the cathode sample, we next look at case III. The CBD-pervaded sub-volume consists of 39.7 vol% solid phase and 60.3 vol% void space. Assuming case III as representative of the CBD porosity, the space occupied by the porous CBD in case I must have the same ratio of solid to void space as case III. From this ratio the void space within the CBD calculates to 17.5 vol% of the reconstruction, which leaves 22.5 vol% of the reconstructed volume to the void space outside the CBD. The porous CBD (solid and void voxels together) then occupies 29.0 vol% of the reconstructed volume. That nearly half of the total pore space (43.8%) is confined within the CBD underscores the high impact of the CBD microstructure on the pore space morphology.

With 60.3% the CBD porosity is considerably above the 47% estimated by Zielke et al.^[19] for the CBD porosity in an LCO cathode. To which extent this divergence reflects differences in electrode preparation conditions that could affect the CBD porosity or advances in the reconstruction process that improve the accuracy of the results (enhanced SEM image quality from resin-filling of the pore space, larger sample volume), is impossible to tell at this point.

2.3.2. Void Space Distribution

The void space distribution in the electrode is determined by the distribution of the two solid components, which differ considerably in morphology. The high degree of connectivity and the complex geometry of the void space preclude a division into individual pores. We describe the void space distribution through chord length distributions (CLDs), which is an automatable method that does not rely on assumptions about the void space geometry and can in principle be applied to any porous medium.^[50–52] The void space is scanned up to the solid-void interface by chords of variable length; collecting and sorting the chords according to their length in a histogram yields the CLD. The mean chord length \bar{l}_c of the CLD is a measure of the average pore size. Figure 4 shows the void space CLDs obtained for cases I–III. The mean chord length \bar{l}_c derived from each CLD is listed in Table 3.

The CLDs are used first to check whether the resolution limits of the reconstruction were chosen correctly at both boundaries. According to the CLD for case I, the average pore size in the cathode is $\bar{l}_c = 1.04 \mu\text{m}$, which agrees with our estimate of 1.0 μm for the discriminate feature size in the void phase on which the edge lengths for the reconstructed volume had been based. According to the CLD for case III, the average pore size within the CBD is $\bar{l}_c = 0.44 \mu\text{m}$ and thus 22-times the tomographic slice thickness of 20 nm. The reconstruction's

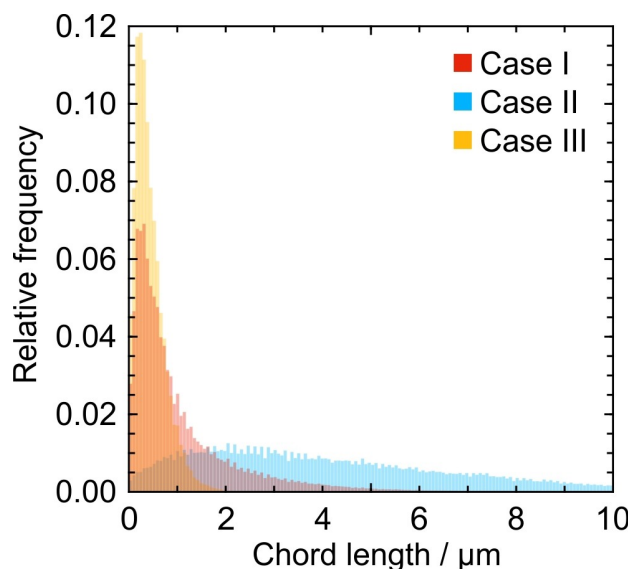


Figure 4. CLDs obtained from different representations of the physical reconstruction describe the void space distribution as defined by solid AM and CBD phases (case I), solid AM phase (case II), and solid CBD phase (case III).

resolution limits thus conform to the requisites for an accurate representation of the electrode's pore space.

The void space CLDs for the three cases are very different from each other. Close inspection of the void space CLD for case I reveals a shoulder to the right (at $l_c = 0.6 \mu\text{m}$), congruent with a bimodal distribution caused by the size difference between pores within and pores outside the CBD. The void space CLD for case II covers, as expected, much larger chord lengths than the CLD for case I, which is also reflected in a mean chord length of $\bar{l}_c = 4.46 \mu\text{m}$, about four-times the average pore size of $\bar{l}_c = 1.04 \mu\text{m}$ in the three-phase reconstruction. Comparison of the void space CLDs for cases I and II visualizes that the presence of the CBD reduces the global average pore size significantly. The void space CLD for case III contains chord lengths up to $1.5 \mu\text{m}$ and exhibits a mode of $0.28 \mu\text{m}$ and a median of $0.37 \mu\text{m}$. Interestingly, the void space CLDs for cases I and III share the same mode (i.e., the most frequent chord length); the void space CLD for case III, however, contains a considerably larger amount of short chords and features a decidedly smaller mean chord length ($\bar{l}_c = 0.44$ and $1.04 \mu\text{m}$ for cases III and I, respectively). This comparison

shows that smaller pores are found mostly within the CBD, where the average pore size is less than half of the global average pore size.

2.3.3. Surface Area of and Contact Area between Solid AM and CBD Phases

The CBD's role in the electrode is to stabilize the AM particle network and provide electronic conduction between the AM particles. Contact between AM particles and the CBD is therefore necessary, but also reduces the active surface area of the AM particles, where Li^+ charge transfer takes place. The three-phase reconstruction allows a precise calculation of the surface area of the solid phases as well as of the contact area between them. The surface areas of solid AM, solid CBD, and both solid phases together were calculated from the full reconstruction volume using the marching cube algorithm^[53] (see Ref. [54] and the Computational Methods section for more details). Calculation directly from the cuboid voxels overestimates the surface area of curved objects.^[54] The marching cube algorithm approximates the curved surface area by using triangles to interpolate the cuboid-voxel based surface area. The volume-specific surface area was obtained by normalizing all received values to the reconstructed volume. The calculation yielded surface areas of $A_{\text{AM}} = 1.02 \mu\text{m}^{-1}$, $A_{\text{CBD}} = 3.96 \mu\text{m}^{-1}$, and $A_{\text{AM,CBD}} = 4.78 \mu\text{m}^{-1}$. These data show that most of the solid-phase surface area in the electrode stems from the CBD.

The AM-void interface, where Li^+ charge transfer takes place, is defined as the active surface whose area A_{active} is calculated from the volume-specific surface areas of solid AM, solid CBD, and both solid phases together:^[7]

$$A_{\text{active}} = A_{\text{AM}} - \frac{1}{2} (A_{\text{AM}} + A_{\text{CBD}} - A_{\text{AM,CBD}}) \quad (3)$$

A_{active} is $0.92 \mu\text{m}^{-1}$, which corresponds to 90.2% of A_{AM} . Consequently, the contact area between AM and solid CBD is $0.10 \mu\text{m}^{-1}$ (10% of the AM surface area). The 10% blockage of the AM surface area by the solid CBD apparently suffices for mechanical stability of the electrode. This leaves 90% of the AM surface in contact with the liquid electrolyte and thus available for charge transfer reactions, which excludes poor accessibility of the electrolyte-AM interface as a limiting factor to battery operation.

Table 3. Morphological parameters obtained by the RS approach.

	Case I	Case II	Case III
Porosity ϵ	40.0%	51.5%	60.3%
CLD mean chord length \bar{l}_c [μm]	1.04	4.46	0.44
CLD median [μm]	0.64	3.73	0.37
CLD mode [μm]	0.28	2.02	0.28
Fraction of three-branch connections	74.0%	91.0%	77.5%
Fraction of four-branch connections	16.1%	7.2%	15.6%
Fraction of higher-branch connections	9.8%	1.8%	7.0%
Average connectivity Z	3.36	3.11	3.30
τ_{RS}	1.89	1.47	1.96

2.3.4. Void Space Connectivity

The connectivity of the pore space^[55] was analyzed through skeletonization.^[56] Figure S3 shows a 2D representation of the skeleton lines in the void space. The analysis was performed in 3D. Skeletonization reduces the amount of data, but conserves topological properties of the pore space, such as branch lengths, curvature, connectivity, and dead-ends. The nodes in the skeleton are sorted according to how many branches (three, four, or more than four) converge there, whereby a three-branch node represents the minimum degree of connectivity. The connectivity of the pore space is then described by the fraction of three-, four-, and higher-branch nodes and by the average connectivity Z calculated from these fractions.

The connectivity analysis for the three-phase reconstruction (case I) yields a surprisingly high fraction of four-branch and higher nodes (~25%), resulting in an average connectivity of $Z=3.36$ (Table 3). Similar connectivity values have been found for the macropore space of silica monoliths, whose pore space interconnectivity is one of their main advantages as support structures for chromatographic separations and heterogeneous catalysis.^[55,56] Comparison with the results of the connectivity analysis for cases II and III clearly shows that the high connectivity of the electrode's pore space is owed mainly to the CBD. The irregularly shaped AM particles form large pores with few interconnections. The void space between the AM particles (case II) contains few ($\leq 9\%$) four-branch or higher nodes, resulting in a low average connectivity of $Z=3.11$. This contrasts with the CBD (case III), for which the connectivity analysis returns a considerable fraction of four-branch and higher nodes (~23%), yielding an average connectivity of $Z=3.30$. These data reveal the CBD as a complex, strongly interconnected pore network that dominates the overall pore space morphology of the electrode.

For those interested in morphological analysis tools, an analysis of the pore tortuosity based on the skeleton lines is provided in the Supporting Information (Section S4). The skeleton-based analysis cannot take constrictivities into account, which is why the resulting geometric tortuosity values for cases I–III do not reflect the transport properties of the respective pore spaces. The accurate characterization of transport properties requires pore-scale diffusion simulations, as shown in the next section.

2.4. Pore-Scale Diffusion Simulations

Diffusion in the void space of cases I–III was numerically simulated using a random-walk particle tracking technique^[58] (see Ref. [28] for further details), where passive, point-like tracers are randomly distributed in the void space. All tracers execute random jumps at each time step. The random displacement of each tracer is recorded and a time-dependent diffusion coefficient $D(t)$ calculated from the individual tracer displacements. The transient diffusion coefficient $D(t)$ eventually reaches its asymptotic, long-time limit D_{eff} (Figure S5). The ratio of the bulk diffusion coefficient D_{bulk} and D_{eff} is the diffusive

tortuosity, designated as τ_{RS} to indicate its derivation by the RS approach. τ_{RS} reflects the complete morphology of the pore space, including constrictivities.

The diffusion simulations deliver a value of $\tau_{\text{RS}}=1.89$ for the three-phase reconstruction (case I) compared with only $\tau_{\text{RS}}=1.47$ for case II (Table 3). The large tortuosity difference cannot be solely attributed to the ~10% porosity difference between cases I and II. Such a large impact of the porosity on the tortuosity is not supported by tortuosity-porosity correlations for the interstitial pore space in consolidated particulate matter.^[59] The large tortuosity of case I is mainly caused by the increased microstructural heterogeneity of the pore space, which comes mostly from the CBD. This becomes clear from considering case III. Although a high porosity of 60% is reached within the CBD, the tortuosity exhibits a high value of $\tau_{\text{RS}}=1.96$. The complex, meandering pore network inside the CBD, including constrictivities, significantly hinders diffusive transport, because the high surface area translates into more wall contacts. The CBD contribution is critical to the overall ionic tortuosity of the electrode as 43.8% of the global porosity are located within the CBD. This analysis demonstrates that transport properties of the electrolyte-filled pore space in battery electrodes cannot be correctly assessed without explicit consideration of the CBD morphology.

3. Discussion

The tortuosity obtained for the three-phase reconstruction (case I) from the RS approach ($\tau_{\text{RS}}=1.89$) differs by a factor of 1.2 from the electrochemically determined tortuosity ($\tau_{\text{EIS}}=2.31$). The tortuosity value for case II ($\tau_{\text{RS}}=1.47$) deviates from the electrochemically determined tortuosity by a factor of 1.6. This emphasizes that only three-phase reconstructions with a sufficiently high resolution of the CBD adequately represent the transport properties of the porous electrode. Still, EIS experiments in the framework of the TLM better reflect the actual conditions in the electrode. Since the measurements are conducted under blocking conditions (100% state-of-charge), no charge transfer occurs at the interface between the AM particles and electrolyte. Ions migrate in the electrolyte and a double layer is formed at the surface of the electronically conducting particles; both processes are considered in the TLM. The fact that τ_{EIS} approaches τ_{RS} (case I) quite closely may originate in the actual electrode morphology. A relatively loose packing of the AM particles generates a highly interconnected interparticle void space (cf. Table 3). As has been shown by Nguyen et al.,^[60] when pore networks are highly percolated and contain a small fraction of dead-end pores (like the void space between loosely packed particles), the latter have a negligible effect on the tortuosity when EIS measurements are considered, which will provide good agreement with tortuosities from diffusion studies. The remaining difference between τ_{EIS} and τ_{RS} from the three-phase reconstruction can have several origins. One possible source are the different comparison volumes. The RS approach investigates a representative volume taken from the bulk section of the electrode, whereas EIS measurements

probe the entire electrode including its edge regions and, therefore, possible porosity gradients across the electrode formed during slurry drying. Another possible source lies in the applicability of the TLM (which assumes straight, cylindrical pores) to the complex pore network found in electrodes. Therefore, RS-derived as well as EIS-derived tortuosity values could reflect the limitations of each method to an extent that is difficult to estimate.

The results of this study show the decisive influence of the CBD morphology on the overall void space distribution in and thus the transport properties of the porous electrode. Commercial battery electrodes have much lower porosities (20–27%) than the investigated cathode sample (40.8%).^[7] Assuming the CBD is not much compacted by calendaring, commercial electrodes can thus be expected to contain a larger fraction of the total porosity inside the CBD than the investigated sample. The influence of the CBD morphology on the transport properties of porous electrodes is therefore possibly still underestimated by the investigated sample. Even for electrodes that contain a smaller CBD volume fraction than the investigated sample, a significant influence of the CBD microstructure on overall ion transport is highly probable.

Explicit consideration of the CBD morphology is indispensable to capture the transport-relevant microstructural properties of porous electrodes. The ionic tortuosity of battery electrodes then should be determined over a wide porosity range by EIS and the RS approach to eventually arrive at a more accurate porosity-tortuosity correlation and quantify how electrode formulation impacts CBD porosity and the overall ionic tortuosity. In a first step, the values found to characterize CBD morphology may serve as input parameters for studies that incorporate the actual electrode manufacturing process^[21] and, in a second step, the entire reconstruction could be used as realistic geometrical model in full-cycle simulations, including charge transfer reactions at the electrolyte-AM interface, to investigate the influence of the CBD on the overall battery performance.

4. Conclusions

This study contains the first high-resolution, physical reconstruction of a morphologically representative volume of an LCO cathode with resolved porous CBD. The reconstruction shows that the porous CBD spans much of the space between the AM particles. Contact between solid CBD and AM particles blocks 10% of the AM surface, which excludes charge transfer as a limiting factor to battery operation. The porous CBD occupies a much smaller volume fraction than the AM phase (29.0% vs 48.5%, respectively), but contains 43.8% of the total pore space. The presence of the CBD decreases the average pore size and increases tortuosity significantly. This means that Li⁺ transport in the electrolyte-filled pore space of the electrode is limited by the morphology of the porous CBD. The tortuosity value obtained from pore-scale diffusion simulations in the three-phase reconstruction of the cathode approaches the tortuosity values determined for comparable cathode samples

by EIS experiments in the framework of the TLM. This proves that resolving the porous CBD within a representative reconstructed volume of the electrode is necessary to reproduce experimentally determined tortuosity values and thus to obtain transport-relevant morphological information about porous electrodes by the RS approach.

Experimental Section

Cathode Materials

LiCoO₂ (LCO) was purchased from Alfa Aesar (Kandel, Germany), Super C65 carbon black from Timcal (Bodio, Switzerland), polyvinylidene fluoride (PVDF) binder from Solvay (Hannover, Germany), and *N*-Methyl-2-pyrrolidone (NMP) from Alfa Aesar. Whatman GF/A glass microfiber filters (GE Healthcare, Buckinghamshire, United Kingdom) were used as separators. Lithium metal foil was received from Albemarle (Frankfurt, Germany). The liquid electrolyte EC/EMC 50:50 + 1 M LiPF₆ ($\sigma_{\text{bulk}} = 7.93 \text{ mS cm}^{-1}$) was purchased from Sigma-Aldrich (Steinheim, Germany).

Cathode Preparation

For a slurry with 60% solid content consisting of 90/5/5 (w/w/w) AM/carbon black/binder, the binder was first dissolved in NMP at 40 °C before LCO particles and carbon black were added gradually. The slurry was mixed with a T 25 disperser (IKA, Staufen, Germany) and applied to an aluminum foil using a ZAA 2300 automatic film applicator (Zehntner, Sissach, Switzerland). The gap height of the applicator was set to 400 μm . The film was dried overnight at 80 °C. The film was calendared at 80 °C using a hot rolling press (MTI, Richmond, CA) to adjust the porosity to 40%. Disc electrodes with a radius of 0.6 cm were cut from the calendared film for EIS measurements, battery cycling, and FIB-SEM tomography.

Electrochemical Impedance Spectroscopy

Electrodes were measured in a symmetrical set-up at 100% state-of-charge using a TSC battery cell (rhd instruments, Darmstadt, Germany). The electrodes were spaced by three separators and soaked with 120 μl electrolyte. The cells were equilibrated overnight at room temperature. Measurements were performed in a two-electrode set-up by using a Multi Autolab/M101 equipped with a FRA32 M impedance module (Metrohm Autolab BV, Utrecht, The Netherlands) in a range from 10⁵ Hz to 10⁻¹ Hz with an AC amplitude of 10 mV. The resistance of the liquid electrolyte was subtracted for better comparability of the impedance spectra. The TLM was fitted to the spectra using the analysis software RelaxIS 3.0 (rhd instruments).

Battery Cycling

The battery cycling was performed using a TSC battery cell (rhd instruments). The LCO cathode exhibited a loading of 34.0 mg cm⁻² and a height of 130 μm . The cell (LCO cathode|separators soaked with electrolyte|Li) was assembled in an argon-filled glove box (UniLab, MBraun, Germany; $x_{\text{H}_2\text{O}} < 1 \text{ ppm}$, $x_{\text{O}_2} < 1 \text{ ppm}$). Galvanostatic cycling was performed in a two-electrode setup using a Multi Autolab M101 (Metrohm, Filderstadt, Germany) with a C-rate of 0.1 C between 3.8 V and 4.0 V (Figure S1).

FIB-SEM Serial Sectioning

First, the void space of the cathode was filled by a two-part silicone resin (Elastosil RT 604, Wacker, Munich, Germany). Three drops of the resin were applied to the sample under vacuum (at ~5 mbar) followed by exposure to vacuum for another hour. After curing for 24 h, the sample was embedded in epoxy resin using a 5/2 (w/w) mixture of Specifix Resin and Specifix-40 Curing Agent (Struers, Ballerup, Denmark) and cured for another 24 h at room temperature. The embedded sample was cut, its cross section polished with sandpaper and then sputtered with gold for 30 s at 30 mA.

A Strata 400S dual-beam FIB-SEM system (FEI/ThermoFisher Scientific, Hillsboro, OR) was used for sample preparation and serial sectioning afterwards. The volume-of-interest was defined in the midsection of the electrode to reconstruct bulk properties and exclude boundary effects in later analyses. A protective platinum layer was deposited on top of the volume-of-interest to reduce curtaining effects. The focused Ga⁺ beam was operated at 30 kV with a current of 21 nA to create a U-shaped trench around the volume-of-interest and a current of 6.5 nA for slicing. The image stack was acquired using the Slice&View package of the instrument software. For this purpose, SEM images were taken at 2 kV collecting backscattered electrons (BSE) with the through-the-lens detector (TLD) in immersion mode (a higher resolution mode of the instrument). The final 8-bit image stack (file size: 5.1 GB) contained 985 slices at a pixel size of 13.9 × 13.9 nm² and 20.0 nm spacing in milling direction.

Computational Methods

Physical Reconstruction

First, the slices were aligned by means of the StackReg^[61] plugin in ImageJ Fiji.^[62] The inclined SEM viewing angle of 52° was corrected in Fiji by rescaling the voxels. Intensity gradients from shadowing were normalized in the three spatial directions by using Visual C# scripts. Shadowing is caused by the trench around the volume-of-interest and by re-deposited material that accumulates during the experiment and blocks electrons on their way to the detector. Curtaining artifacts were removed using the wavelet-Fourier filter approach proposed in Münch et al.^[63] For the wavelet decomposition, a Daubechies 8 wavelet^[64] was used. The decomposition level was chosen as $L=5$ and the damping coefficient was set to $\sigma=10$. A Gaussian filter was applied for noise removal and the contrast was enhanced using Fiji. As the curtaining was more severe in the bottom part of the image, the image quality in this region remained reduced even after application of the decurtaining filter, resulting in a loss of contrast between the different phases in this area. This made segmentation with global or local color threshold values difficult, so that we relied on a machine learning approach for this critical step of the reconstruction process. We used the software Zeiss ZEN Intellesis (Oberkochen, Germany), which is based on trainable deep-learning algorithms. The segmentation algorithm yielded good results, which were first evaluated by visual comparison. Charging effects within the silicone resin resulted in some void voxels being wrongly assigned to the AM phase, which was corrected semi-manually using the 3D watershed segmentation of the MorphoLibJ plugin^[65] to identify these areas. The resulting 8-bit image stack constituted case I. Case II was derived from case I through reassigning solid CBD voxels as void voxels. For case III, we visually identified the largest section of porous CBD in the reconstructed volume and extracted the maximum possible cuboid from this section.

Chord Length Distribution

A statistically significant number of 10⁶ seed points was randomly distributed in the void space of cases I–III. From each seed point, 26 vectors that pointed in directions induced by the 26 neighborhood in the voxel lattice were projected until the vectors hit the solid-void interface. Opposing vectors form a chord. Chords that reached the boundary of the reconstruction were discarded. Valid chords were collected and sorted by length into a histogram.

Calculation of the Surface Area

The marching cube algorithm^[53] considers the surroundings of the voxels and approximates the area at the solid-void interface by triangles. The algorithm assesses a set of eight voxels at a time, whereby each voxel is considered a cube vertex. The color value of the voxel determines whether the vertex belongs to the solid phase or to the void space, resulting in 15 different cube configurations. The cube configuration in turn results in a certain triangle configuration of up to four triangles per cube. The areas of the triangles are summed up into the total area. A C++ implementation^[66] of the algorithm was adapted for the analysis. The resulting surface area was divided by the volume of the reconstruction ($1.3 \times 10^4 \mu\text{m}^3$) to obtain the volume-specific surface area.

Connectivity Analysis

The skeletonization of the void space was executed in Fiji using the “Skeletonize3D” plugin. The average connectivity Z was calculated by determining the number of branches meeting at each node. Dead-end nodes connected to only one branch were not considered. The average connectivity Z was calculated as the sum of the weighted ratios of the number of three-branch nodes n_t , four-branch nodes n_q , and higher-level branch nodes n_x to the total number of nodes n_j :^[55]

$$Z = 3 \frac{n_t}{n_j} + 4 \frac{n_q}{n_j} + 5 \frac{n_x}{n_j} \quad (4)$$

Diffusion Simulation

Diffusion in the void space of cases I–III was numerically simulated using the random-walk particle-tracking (RWPT) technique.^[58,67,68] 10⁶ inert (non-reactive and non-adsorbing) tracers were randomly distributed in the void space. The random displacement Δr of all tracers by molecular diffusion was calculated for each time step:

$$\Delta r = \gamma \sqrt{6D_{\text{bulk}} \Delta t} \quad (5)$$

Here γ represents a spatial vector and D_{bulk} the tracer diffusion coefficient. Orientation and length of γ are random, determined by a Gaussian function. The time steps were chosen such that the mean diffusive displacement remained below $\Delta h/10$ (with Δh denoting the pixel resolution of 13.9 nm). Jumps leading out of the reconstruction volume were treated by mirror boundary conditions, whereby tracers continue their path mirrored in the original domain.^[68] The interaction with the solid-void interface was simulated by a multiple-rejection boundary condition,^[69] whereby when a tracer crosses the boundary during a jump, this jump is discarded and recalculated until a valid jump is made. The time-dependent diffusion coefficient $D(t)$ was calculated as

$$D(t) = \frac{1}{6N} \frac{d}{dt} \sum_{i=1}^N [\Delta r_i(t)]^2 \quad (6)$$

where $\Delta r_i(t)$ is the displacement of the i -th tracer at time t (Figure S5). The effective diffusion coefficient D_{eff} was taken from the asymptotic, long-time limit of $D(t)$ and the ionic tortuosity τ_{RS} calculated as

$$\tau_{\text{RS}} = \frac{D_{\text{bulk}}}{D_{\text{eff}}} \quad (7)$$

The accuracy of this modeling approach has been confirmed by comparing D_{eff} -values simulated in regular (simple cubic and face-centered cubic) arrays of spheres^[70,71] with values calculated using the analytical approach.^[72] Among the advantages of the employed RWPT technique are conservation of mass, absence of numerical dispersion, simplicity of program realization, and straightforward parallelization. Consequently, the program realization of the RWPT algorithm was implemented as parallel code in C language using the Message Passing Interface (MPI) standard on a supercomputing platform. All numerical codes and their description can be found in the Supporting Information of Ref. [68].

Acknowledgements

This work was supported by the Karlsruhe Nano Micro Facility (KNMF) at the Karlsruhe Institute of Technology (Karlsruhe, Germany) under the KNMF long-term user proposal 2020-024-029294. We thank Janika Hochstrasser for carrying out the numerical simulations. Open access funding enabled and organized by Projekt DEAL.

Conflict of Interest

The authors declare no conflict of interest.

Keywords: electrochemistry · electron microscopy · ion transport · nanoscale tomography · physical reconstruction

- [1] T. Kim, W. Song, D.-Y. Son, L. K. Ono, Y. Qi, *J. Mater. Chem. A* **2019**, *7*, 2942.
- [2] J. B. Goodenough, K.-S. Park, *J. Am. Chem. Soc.* **2013**, *135*, 1167.
- [3] H. Sun, J. Zhu, D. Baumann, L. Peng, Y. Xu, I. Shakir, Y. Huang, X. Duan, *Nat. Rev. Mater.* **2019**, *4*, 45.
- [4] L. Pfaffmann, S. Jaiser, M. Müller, P. Scharfer, W. Schabel, W. Bauer, F. Scheiba, H. Ehrenberg, *J. Power Sources* **2017**, *363*, 460.
- [5] J. Chen, J. Liu, Y. Qi, T. Sun, X. Li, *J. Electrochem. Soc.* **2013**, *160*, A1502.
- [6] L. Zielke, T. Hutzenlaub, D. R. Wheeler, I. Manke, T. Arlt, N. Paust, R. Zengerle, S. Thiele, *Adv. Energy Mater.* **2014**, *4*, 1301617.
- [7] L. Almar, J. Joos, A. Weber, E. Ivers-Tiffée, *J. Power Sources* **2019**, *427*, 1.
- [8] G. Liu, H. Zheng, S. Kim, Y. Deng, A. M. Minor, X. Song, V. S. Battaglia, *J. Electrochem. Soc.* **2008**, *155*, A887.
- [9] M. Müller, L. Pfaffmann, S. Jaiser, M. Baunach, V. Trouillet, F. Scheiba, P. Scharfer, W. Schabel, W. Bauer, *J. Power Sources* **2017**, *340*, 1.
- [10] G.-W. Lee, J. H. Ryu, W. Han, K. H. Ahn, S. M. Oh, *J. Power Sources* **2010**, *195*, 6049.
- [11] S.-L. Chou, Y. Pan, J.-Z. Wang, H.-K. Liu, S.-X. Dou, *Phys. Chem. Chem. Phys.* **2014**, *16*, 20347.
- [12] J. Landesfeind, A. Eldiven, H. A. Gasteiger, *J. Electrochem. Soc.* **2018**, *165*, A1122.

- [13] R. Dominko, M. Gaberscek, J. Drofenik, M. Bele, S. Pejovnik, J. Jamnik, *J. Power Sources* **2003**, *119–121*, 770.
- [14] J. K. Mayer, L. Almar, E. Aslybekov, W. Haselrieder, A. Kwade, A. Weber, H. Nirschl, *Energy Technol.* **2020**, *8*, 1900161.
- [15] R. Morasch, J. Landesfeind, B. Suthar, H. A. Gasteiger, *J. Electrochem. Soc.* **2018**, *165*, A3459.
- [16] T. Hutzenlaub, A. Asthana, J. Becker, D. R. Wheeler, R. Zengerle, S. Thiele, *Electrochem. Commun.* **2013**, *27*, 77.
- [17] Z. Liu, Y.-C. K. Chen-Wiegart, J. Wang, S. A. Barnett, K. T. Faber, *Microsc. Microanal.* **2016**, *22*, 140.
- [18] S. Vierrath, L. Zielke, R. Moroni, A. Mondon, D. R. Wheeler, R. Zengerle, S. Thiele, *Electrochem. Commun.* **2015**, *60*, 176.
- [19] L. Zielke, T. Hutzenlaub, D. R. Wheeler, C.-W. Chao, I. Manke, A. Hilger, N. Paust, R. Zengerle, S. Thiele, *Adv. Energy Mater.* **2015**, *5*, 1401612.
- [20] T. Hutzenlaub, S. Thiele, N. Paust, R. Spotnitz, R. Zengerle, C. Walchshofer, *Electrochim. Acta* **2014**, *115*, 131.
- [21] M. Chouchane, A. Rucci, T. Lombardo, A. C. Ngandjong, A. Franco, *J. Power Sources* **2019**, *444*, 227285.
- [22] A. Shodiev, E. N. Primo, M. Chouchane, T. Lombardo, A. C. Ngandjong, A. Rucci, A. Franco, *J. Power Sources* **2020**, *454*, 227871.
- [23] A. C. Ngandjong, T. Lombardo, E. N. Primo, M. Chouchane, A. Shodiev, O. Arcelus, A. Franco, *J. Power Sources* **2021**, *485*, 229320.
- [24] T.-T. Nguyen, J. Villanova, Z. Su, R. Tucoulou, B. Fleutot, B. Delobel, C. Delacourt, A. Demortière, *Adv. Energy Mater.* **2021**, *11*, 2003529.
- [25] G. Gaiselmann, M. Neumann, V. Schmidt, O. Pecho, T. Hocker, L. Holzer, *AIChE J.* **2014**, *60*, 1983.
- [26] O. Stenzel, O. Pecho, L. Holzer, M. Neumann, V. Schmidt, *AIChE J.* **2016**, *62*, 1834.
- [27] D. Hlushkou, A. E. Reising, N. Kaiser, S. Spannenberger, S. Schlabach, Y. Kato, B. Roling, U. Tallarek, *J. Power Sources* **2018**, *396*, 363.
- [28] M. Kroll, D. Hlushkou, S. Schlabach, A. Hölzel, B. Roling, U. Tallarek, *J. Electrochem. Soc.* **2018**, *165*, A3156.
- [29] A. P. Cocco, G. J. Nelson, W. M. Harris, A. Nakajo, T. D. Myles, A. M. Kiss, J. J. Lombardo, W. K. S. Chiu, *Phys. Chem. Chem. Phys.* **2013**, *15*, 16377.
- [30] J. Conder, C. Marino, P. Novák, C. Villevieille, *J. Mater. Chem. A* **2018**, *6*, 3304.
- [31] P. R. Munroe, *Mater. Charact.* **2009**, *60*, 2.
- [32] G. Möbus, B. J. Inkson, *Mater. Today* **2007**, *10*, 18.
- [33] A. Ul-Hamid, *A Beginners' Guide to Scanning Electron Microscopy*, Springer International Publishing, Cham, **2018**.
- [34] J. Landesfeind, M. Ebner, A. Eldiven, V. Wood, H. A. Gasteiger, *J. Electrochem. Soc.* **2018**, *165*, A469.
- [35] B. L. Trembacki, A. N. Mistry, D. R. Noble, M. E. Ferraro, P. P. Mukherjee, S. A. Roberts, *J. Electrochem. Soc.* **2018**, *165*, E725.
- [36] L. S. Kremer, A. Hoffmann, T. Danner, S. Hein, B. Prifling, D. Westhoff, C. Dreer, A. Latz, V. Schmidt, M. Wohlfahrt-Mehrens, *Energy Technol.* **2020**, *8*, 1900167.
- [37] S. Hein, T. Danner, D. Westhoff, B. Prifling, R. Scurtu, L. Kremer, A. Hoffmann, A. Hilger, M. Osenberg, I. Manke, M. Wohlfahrt-Mehrens, V. Schmidt, A. Latz, *J. Electrochem. Soc.* **2020**, *167*, 13546.
- [38] S. R. Daemi, C. Tan, T. Volkenandt, S. J. Cooper, A. Palacios-Padros, J. Cookson, D. J. L. Brett, P. R. Shearing, *ACS Appl. Mater. Interfaces* **2018**, *1*, 3702.
- [39] T. Hutzenlaub, S. Thiele, R. Zengerle, C. Ziegler, *J. Electrochem. Soc.* **2012**, *15*, A33.
- [40] R. de Levie, in *Advances in Electrochemistry and Electrochemical Engineering* (Ed.: P. Delahay), Interscience, New York, **1967**, Vol. 6, pp. 329–397.
- [41] A. Lasia, *Electrochemical Impedance Spectroscopy and its Applications*, Springer, New York, **2014**.
- [42] N. Ogihara, Y. Itou, T. Sasaki, Y. Takeuchi, *J. Phys. Chem. C* **2015**, *119*, 4612.
- [43] J. Landesfeind, J. Hattendorff, A. Ehrl, W. A. Wall, H. A. Gasteiger, *J. Electrochem. Soc.* **2016**, *163*, A1373.
- [44] C. Chen, J. Liu, K. Amine, *J. Power Sources* **2001**, *96*, 321.
- [45] E. J. Cheng, N. J. Taylor, J. Wolfenstine, J. Sakamoto, *J. Asian Ceram. Soc.* **2017**, *5*, 113.
- [46] D. Boudouris, L. Constantinou, C. Panayiotou, *Fluid Phase Equilib.* **2000**, *167*, 1.
- [47] T. Prill, K. Schladitz, *Scanning* **2013**, *35*, 189.
- [48] T. Müllner, A. Zankel, F. Svec, U. Tallarek, *Mater. Today* **2014**, *17*, 404.
- [49] M. D. Uchic, L. Holzer, B. J. Inkson, E. L. Principe, P. Munroe, *MRS Bull.* **2007**, *32*, 408.
- [50] A. Çeçen, E. A. Wargo, A. C. Hanna, D. M. Turner, S. R. Kalidindi, E. C. Kumbur, *J. Electrochem. Soc.* **2012**, *159*, B299.

- [51] D. Stoeckel, C. Kübel, M. O. Loeh, B. M. Smarsly, U. Tallarek, *Langmuir* **2015**, *31*, 7391.
- [52] H. Reinhardt, M. Kroll, S. L. Karstens, S. Schlabach, N. A. Hampp, U. Tallarek, *Adv. Mater. Interfaces* **2021**, *8*, 2000253.
- [53] W. E. Lorensen, H. E. Cline, *ACM SIGGRAPH Comput. Graph.* **1987**, *21*, 163.
- [54] J. Joos, T. Carraro, M. Ender, B. Rüger, A. Weber, E. Ivers-Tiffée, *ECS Trans.* **2011**, *35*, 2357.
- [55] K. Hormann, V. Baranau, D. Hlushkou, A. Höltzel, U. Tallarek, *New J. Chem.* **2016**, *40*, 4187.
- [56] D. Enke, R. Gläser, U. Tallarek, *Chem. Ing. Tech.* **2016**, *88*, 1561.
- [57] T. C. Lee, R. L. Kashyap, C. N. Chu, *CVGIP: Graphical Models and Image Processing* **1994**, *56*, 462.
- [58] F. Delay, P. Ackerer, C. Danquigny, *Vadose Zone J.* **2005**, *4*, 360.
- [59] B. Ghanbarian, A. G. Hunt, R. P. Ewing, M. Sahimi, *Soil Sci. Soc. Am. J.* **2013**, *77*, 1461.
- [60] T.-T. Nguyen, A. Demortière, B. Fleutot, B. Delobel, C. Delacourt, S. J. Cooper, *NPJ Computational Materials* **2020**, *6*, 123.
- [61] P. Thévenaz, U. E. Ruttimann, M. Unser, *IEEE Trans. Image Process.* **1998**, *7*, 27.
- [62] J. Schindelin, I. Arganda-Carreras, E. Frise, V. Kaynig, M. Longair, T. Pietzsch, S. Preibisch, C. Rueden, S. Saalfeld, B. Schmid, J.-Y. Tinevez, D. J. White, V. Hartenstein, K. Eliceiri, P. Tomancak, A. Cardona, *Nat. Methods* **2012**, *9*, 676.
- [63] B. Münch, P. Trtik, F. Marone, M. Stampanoni, *Opt. Express* **2009**, *17*, 8567.
- [64] I. Daubechies, *Ten Lectures on Wavelets*, SIAM, Philadelphia, PA, **1992**.
- [65] D. Legland, I. Arganda-Carreras, P. Andrey, *Bioinformatics* **2016**, *32*, 3532.
- [66] P. Bourke, "Polygonising a scalar field", <http://paulbourke.net/geometry/polygonise/>, **1994**.
- [67] J. Salles, J.-F. Thovert, R. Delannay, L. Prevors, J.-L. Auriault, P. M. Adler, *Phys. Fluids A* **1993**, *5*, 2348.
- [68] D. Hlushkou, A. Svidrytski, U. Tallarek, *J. Phys. Chem. C* **2017**, *121*, 8416.
- [69] P. Szymczak, A. J. C. Ladd, *Phys. Rev. E* **2003**, *68*, 036704.
- [70] H. Liasneuski, D. Hlushkou, S. Khirevich, A. Höltzel, U. Tallarek, S. Torquato, *J. Appl. Phys.* **2014**, *116*, 034904.
- [71] A. Daneyko, D. Hlushkou, V. Baranau, S. Khirevich, A. Seidel-Morgenstern, U. Tallarek, *J. Chromatogr. A* **2015**, *1407*, 139.
- [72] M. H. Bles, J. C. Leyte, *J. Colloid Interface Sci.* **1994**, *166*, 118.

Manuscript received: February 25, 2021

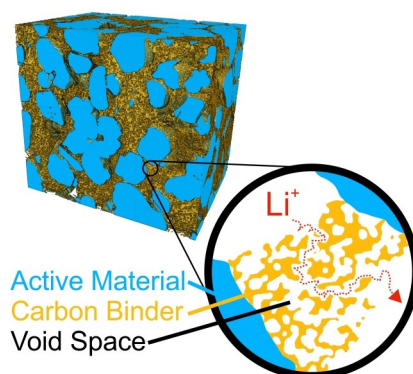
Revised manuscript received: March 25, 2021

Accepted manuscript online: April 9, 2021

Version of record online: ■■■, ■■■■

ARTICLES

Limiting domain: The multiscale, multiphase reconstruction of a lithium-ion battery cathode resolves the convoluted pore space within the carbon binder domain (CBD). Morphological analysis and pore-scale diffusion simulations identify the CBD as the limiting factor for Li^+ transport in the liquid electrolyte. The CBD microstructure must be explicitly considered to recover the electrochemically determined ionic tortuosity values of porous electrodes.



M. Kroll, S. L. Karstens, M. Cronau, Dr. A. Höltzel, Dr. S. Schlabach, N. Nobel, Prof. C. Redenbach, Prof. B. Roling, Prof. U. Tallarek**

1 – 12

Three-Phase Reconstruction Reveals How the Microscopic Structure of the Carbon-Binder Domain Affects Ion Transport in Lithium-Ion Batteries

